

**Towards an Integrated Texture Toolkit, 1: Unveiling the Complex Relationship Between Crystal Size, Shape, and Fabric in EBSD Data**

Ryan M., Currier\*<sup>1</sup>, Tushar Mittal<sup>2</sup>, Paulo J., Hidalgo<sup>3</sup>

**\*Corresponding Author**, rcurrier@westga.edu

1. University of West Georgia, Department of Natural Sciences, 1601 Maple St., Carrollton, GA, USA, 30118
2. Pennsylvania State University. Department of Geosciences, 116 Deike Building, University Park, PA 16802
3. Georgia State University, Department of Geosciences, 38 Peachtree Center Ave. SE 7th Floor Suite 730, Atlanta, GA 30303

**This manuscript is a non-peer reviewed preprint submitted to EarthArXiv. This manuscript has been submitted to Contributions in Mineralogy and Petrology**

## **ABSTRACT**

Rock textures observed via thin section are skewed from their true 3D nature. This is due to a variety of cut effects—artifacts that are introduced due to the lower dimensional nature of the thin section relative to the rock. Typically, these methods invert crystal shape and crystal size, but with each process performed separately and in sequence. With the ongoing adoption of electron backscatter diffraction (EBSD) by petrologists, an additional data stream has now become available: the 3D orientation of 2D grain sections. For EBSD analysis, no stereological corrections are typically applied for interpreting the data. In this study, we test whether this orientational information is also skewed due to a fabric cut effect. We test this by numerically generating synthetic crystal datasets representative of a number of crystal shapes and population sizes. We find that EBSD orientational data does have a fabric cut effect since crystals oriented with long axes perpendicular to the thin section are more likely to be sampled compared to those with long axes oriented parallel to it. This effect needs to be accounted for to accurately interpret the true 3D fabric. Towards this end, we develop a method of inverting cut fabrics which provides robust error estimations and show its accuracy using a range of synthetic examples. When applied to natural samples, which are inherently more complex than the simplified, synthetic samples, we find that the inversion process does not always produce geologically plausible results. To more faithfully correct for the different cut effects, we argue that the stereological inversion process should not be performed separately or sequentially, as is commonly done at present. Instead, we need a new textural toolkit framework to correct for crystal shape, size, and orientation simultaneously with accurate uncertainty estimates.

## **1) Introduction**

Rock texture encapsulates the spatial and geometric characteristics elements within the rock. Particle shape, size, and orientation are all examples of textural features. The textural information is, in turn, a critical observational input for characterizing the physical properties of geomaterials and understanding the processes associated with forming the constituent minerals. For instance, rock textural features encode many physical properties of the rock, such as seismic wave speed (Satsukawa et al. 2013; Frothingham et al. 2023), thermal expansivity (Gibert et al. 2003), fluid permeability (Urumovic and Urumovic 2014), and mechanical strength (Prikryl 2006). Additionally, in igneous rocks, the mineral grain shape and size are functions of cooling rate (Holness 2014; Mangler et al. 2022; Marsh, 1998), while orientations can encode the kinematic history (e.g. magmatic sense of shear: Vukmanovic et al. 2018; compaction: Bertollett et al. 2019; Jenkins et al. 2022; grain clustering mechanisms: Wieser et al. 2019; Holness et al. 2023). Similar applications can be extended into metamorphic systems with rock fabric encoding the deformation history and behavior (Bernard et al. 2023; Bestmann et al. 2006; Casale et al. 2023; Cross et al. 2017b, Haertel and Herwegh 2014; Fossen and Cavalcante 2017; Koyama et al. 2023; Levy et al. 2023; Li et al. 2023; Rehman et al. 2023; Taylor et al. 2023; Wiesman et al. 2023), impact dynamics recorded in meteorites (Goudy et al. 2023; Forman et al. 2023), fluid reactivity with primary minerals (Andreani et al. 2009; Etschmann et al. 2014; Kang et al. 2010), sedimentary processes (McLaren 1981), as well as biosphere/geosphere interaction (Hemkemeyer et al. 2018).

Historically, most textural analyses have been performed in thin section, by measuring the 2D outlines of the intersection between a crystal and the thin section. This methodology requires little in terms of instrumentation—a petrographic microscope and illustration software—so the entry cost is minimal. Over the past few decades, there have been significant improvements - both on the instrumental side (e.g., digital microscopy, EBSD: electron backscatter diffraction, QEMSCAN: quantitative evaluation of materials by scanning electron microscopy), as well as data analysis methods (e.g., image segmentation, shape and spatial analysis), in characterizing the rock microtexture and rapid processing of large datasets. However, there is still inherently a fundamental challenge with all these

methods of textural analysis on a thin section: converting 2D in-plane measurements to 3D estimates using stereological correction techniques. To overcome this challenge, 3D imaging techniques like X-ray tomography have been developed for textural analysis (Jerram and Higgins 2007; Jerram et al. 2010; Lanzafame et al. 2017; Polacci et al. 2018). However, these techniques are inherently data intensive (both in terms of collection and processing), expensive, and are hence not eminently scalable or easily accessible for the majority of the geoscience community. Thus, 2D thin section analysis remains the dominant and most accessible form of textural analysis.

The challenges associated with accurate stereological (2D to 3D) analysis have been known for decades (Higgins 1994; Howard and Reed 1998; Saltikov 1967; Underwood 1969). Several stereological 2D to 3D correction tools have been developed based on these, especially in the igneous petrology community (e.g., CSDCorrections: Higgins 2000; CSDslice: Morgan and Jerram 2006; ShapeCalc: Mangler et al. 2022). The 2D crystal size is by far the most analyzed parameter, corresponding to the areal intersection of a 3D crystal with the cutting plane of the section. The 3D shape of crystals can be derived from 2D measurements by adopting different stereological approaches. However, these existing tools for stereological corrections are based on several simplifying, but hidden, assumptions which may not be appropriate for each dataset. For instance, analysis methods frequently assume that crystal shape is constant across all crystal sizes, whereas this can potentially vary across the population (Mock and Jerram 2005), or as a function of crystal size (Dunbar et al. 1995; Mangler et al. 2022). Analogously, the tools typically do not provide the full uncertainty covariance matrix between shape, size, and orientation. In addition, these prepacked tools are typically not fully open source, and without access to the underlying code for analysis and synthetic crystal cut generation, significant barriers are present for users to make modifications as needed for their geologic context and datasets.

There is thus a need for an open source, well-documented, validated, and extendable textural analysis toolkit for thin section analysis with two key aims: (I) accurate stereological textural corrections, with associated uncertainties, for shape, size, and orientations, and (II) flexibility to incorporate multiple types of thin section datasets jointly (i.e. electron beam methodologies as well as different optical methodologies such as reflected light with different illumination angles, transmitted light, and cross-polarized with multiple orientations). The need for this textural toolkit is, in particular, becoming increasingly relevant since two mature methodologies are capable of automated grain analysis within the Scanning Electron Microscope (SEM). QEMSCAN utilizes chemical analyses to identify phases, and can produce grain maps on the basis of these chemical differences. Another technique, EBSD, utilizes crystal lattice to identify phase and crystal lattice orientation to segment grains (for review, see: Wilkinson and Britton 2012; Britton et al. 2016). One of the benefits of EBSD analysis is that it can be used for automated grain segmentation based on the principle of localized orientation clustering within a single crystal (Cone et al. 2020). Thus, EBSD datasets address some of the key practical challenges with classical thin section analysis: (a) collecting statistically significant datasets via manual crystal tracing are time consuming, and (b) these datasets are prone to error because crystal boundaries are often subjective, and variance in analyses occurs from person to person.

EBSD, compared to QEMSCAN or traditional optical methods, additionally provides 3D crystal orientations of 2D crystal intersections, yielding a 2.5D map of rock texture. In this study, we focus on EBSD analyses, because the orientation information represents an additional, hitherto unexplored, data stream that can be leveraged to more fully characterize rock texture. In particular, this paper focuses on the following question: What are the (if any) stereological biases that can be present when analyzing the crystal orientation datasets from EBSD? An increasing number of studies are using EBSD for rock textural analysis (Bernard et al. 2023; Bertollett et al. 2019; Casale et al. 2023; Cheadle and Gee 2017; Cross et al. 2017a; Cross et al. 2017b; Forman et al. 2023; Goudy et al. 2023; Henry et al. 2021; Holness et al. 2023; Jenkins et al. 2022; Koyama et al. 2023; Levy et al. 2023; Li et al. 2023; Rehman et al. 2023; Wieser et al. 2019; Wiesman et al. 2023; Vukmanovic et al. 2018; Zavada et al. 2009). However, in contrast to 2D thin

section size-shape analysis, the need for stereological corrections with EBSD orientation datasets hasn't been thoroughly scrutinized. Our study addresses this critical knowledge gap and illustrates that the EBSD data does display a "fabric" cut effect that must be corrected for, especially in samples with weak fabric (e.g., magmatic systems). This illustrates one of the necessary components for a next-generation textural toolkit.

We begin with a brief review of stereological artifacts (section 2), followed by the methodologies employed in EBSD and our modelling (section 3). Following this, we present results from synthetically developed rock textures and develop an inversion algorithm to correct for the fabric-cut effect (section 4). Finally, we apply our methodological approach to a few natural samples and discuss the key challenges to further develop the textural toolkit (section 5).

## 2) Background

A 2D slice of a 3D object represents a loss of dimension, and consequently, loss of information about the 3D structure of the object. The observable data in a 2D slice deviates from that of the true 3D quantity (or likewise 1D slices of 2D shapes). This is known as a *cut effect*. The goal of stereology is to correct for these cut effects, allowing for a more robust interpretation of the 3D characteristics of a sample from a 2D cross-section view. Several cut effects become embedded in the 2D information offered by the cross-section. While these are typically lumped into a catch-all term, *the cut effect*, we unpack this general term and explicitly detail each type:

**(a) Size-Cut Effect:** the apparent size of a cut particle (i.e. crystal, grain, or otherwise) is dependent on the orientation of the particle, as well as its extra-dimensional location relative to the cut. This results in a range of potential apparent sizes for a particle. For a random underlying distribution of particle orientations and centers, the size-cut effect results in a distribution of apparent sizes, even if the underlying size is the same for all particles (Figure 1a). Because the apparent size of a particle offered in a slice can never be larger than the true size of the particle, the size cut effects often makes particles appear smaller than reality.

**(b) Size-Distribution-Cut Effect:** for a unit area or a unit volume, a 1D and 2D cut section respectively is more likely to intersect a large particle than a small particle (Figure 1b). For a distribution of particle sizes, a slice thus disproportionately samples larger particles. This leads to a bias in the measurement particle size distribution in a 2D thin section compared to the 3D size distribution with apparent too many small particles in the measured 2D cut (analogous to 1D).

**(c) Shape-Cut Effect:** Depending on how a particle is sliced, the resulting lower dimension shape is not representative of the true shape of the particle for a large proportion of potential slices. Thus, the measurements of particle shape descriptors such as aspect ratio, ellipticity, particle area, Feret diameter, etc., would also be biased compared to the true 3D distributions. The potential shape-cut effect becomes increasingly large as the particle shape deviates from a sphericity.

**(d) Fabric-Cut Effect:** For a collection of distributed particle orientation, particles are more likely to be intersected when their long axis is perpendicular to the thin section, and less likely when the long axis is in plane with the thin section (Figure 1c). An intersection phase diagram (Figure 1d) can be mapped by varying the distance between particle centers and the cut, then rotating the particles and testing for intersection. In this example, the particles are rectangles (Long: 3, Short: 1), and it can be observed that as the orientation of the rectangle long axis approaches perpendicular to the intersection line, they are sampled by the cut from greater distances. For a uniform distribution of particle orientations and particle centers, the result is an apparent fabric with long axes oriented perpendicular to the cut.

These cut effects do not exist in isolation from each other. Instead, the *overall* cut effect is a function of each cut effect, coupled to the others. If we care about the fabric of the sample as a microstructural quantity, then all cut effects need to be self-consistently accounted for. Even if we use

EBSD which provides crystallographic orientations directly, and hence nominally the micro-textural fabric, *the EBSD results still need to account for the fabric cut effect.*

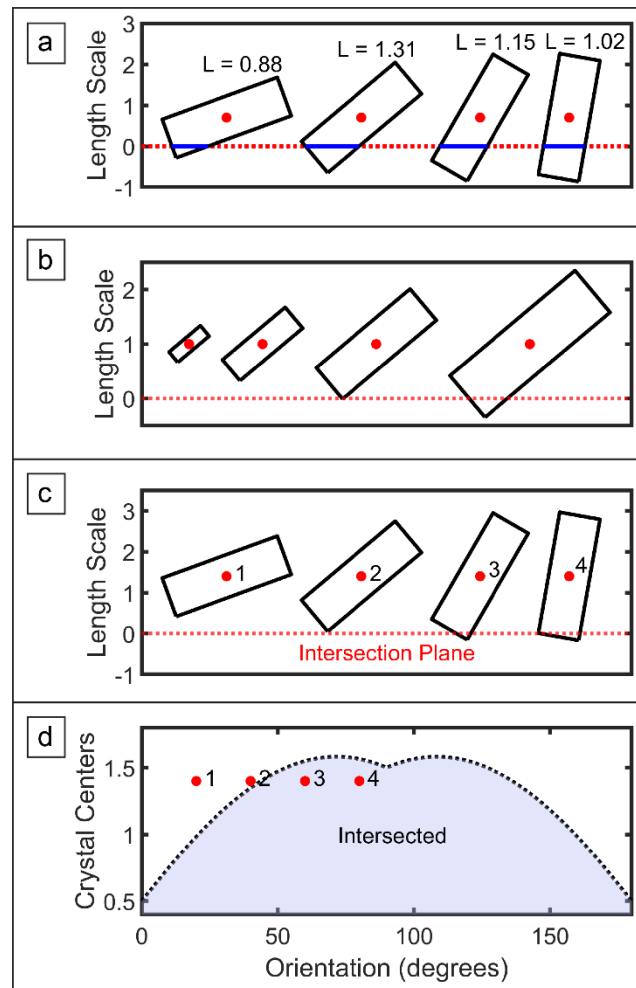


**Fig. 1** Simplified, 2D examples of Cut-Effects. a) Slices of cut shapes are lower dimensional features (here: 1D line segments), which are skewed from the true higher dimensional shape. b) The cut disproportionately samples crystals of different shapes (shown) or sizes (not shown), despite other variables being controlled for. c) The Fabric Cut-Effect is the disproportionate sampling of crystals on the basis of orientation, indicating that the apparent fabric of a slice is skewed from the true higher-dimensional fabric. d) The sampling space for a 2D shape with Long: 3, Short: 1 dependent on shape-cut distance (y-axis) and long axis orientation relative to the cut (x-axis). Numbered points correspond to the oriented shapes in C

Traditional textural analyses correct for cut effects independently. For example, a typical workflow is to first invert for crystal shape (i.e., shape-cut effect, CSDslice: Morgan and Jerram 2006; ShapeCalc: Mangler et al. 2022), then using this as input, invert for crystal size distribution (i.e., size- and size-distribution-cut effects, CSDCorrections: Higgins 2000). While the shape-, size-, and size-distribution-cut effects have been analyzed in previous studies, a careful analysis of the fabric-cut effect and methods to correct for it are currently lacking. The fabric-cut effect forms the basis of this study. An

investigation of the fabric-cut effect is presented here, followed by tools to interpret and process EBSD fabrics. The first tool is a simple method for characterizing fabrics as being either consistent with uniform or non-uniform orientations. The second is a method for inverting the cut effect to construct a representation of the underlying 3D fabric using a synthetic forward modeling approach. As a first approach towards investigating the fabric cut effect, we follow an approach motivated by similar existing methodologies, where the fabric cut effect is solved for independently of the other cut effects and thus assumes that the different cut effects are sequentially separable. Therefore, the hypothesis is: the full cut effect correction ( $f$ ) can be represented as a series of sequential functions:

$$f(shape, size, orient.) = f_x(shape) \times f_y(shape_0, orient.) \times f_z(shape_0, orient_0, size) \quad (1)$$

Where  $f_x$  is the shape cut effect,  $f_y$  is the fabric cut effect with shape fixed, and  $f_z$  is the size and size distribution cut effect with shape and orientation fixed. We test this assumption by developing a method for  $f_y$  and applying it to synthetic and natural samples.

We note that in natural datasets, other effects need to be considered. For example, the spatial interdependence of multiple particle populations leading to correlations and constraints on particle orientation to not physically overlap. A potentially influential effect on results is the number of measured crystals. There is ever only a finite number of measurements of crystals within a single sample, and depending on whether the data is acquired manually or in an automated fashion, the sample size can vary markedly. Thus, the effects of crystal numbers include additional uncertainties in inversion methods when correcting for all the stereological cut effects.

### 3) Methods

Following existing work in this field, we follow the general outline for modelling the cut effect of grain shape (Higgins 1994; Morgan and Jerram 2006; Mangler et al. 2022). At the heart of these 3D shape estimators is a catalog of 2D intersection data from known 3D shapes that have been uniformly rotated and randomly distributed in a volume, such that all particles are free to “miss” the intersection plane, and only 2D data from intersections are collected.

We generate synthetic rock fabric datasets in the MATLAB environment. A key rationale for this choice is that the freely available MTEX toolkit (Bachmann et al. 2010) designed for analyzing EBSD data, is written in the MATLAB environment. Additionally, MTEX has many built-in functions that aid in generating and analyzing synthetic datasets. A user-defined, six-sided crystal shape, tied to crystallographic axes, results in eight vertices of a simple unrotated crystal (Figure 2a). This shape is fixed across all generated crystals. From a prescribed input fabric, discrete rotations are sampled as unit quaternions and applied to the set of unrotated crystals (Figure 2b). A quaternion,  $q$ , can be expressed as a combination of real and complex numbers, usually in the form of:

$$q = a + bi + cj + dk \quad (2)$$

Unit quaternions, which are defined as a quaternion of length = 1, can be rewritten as the combination of a vector,  $V$ , which serves as the axis of rotation, and a rotation magnitude:

$$q = \cos\left(\frac{\theta}{2}\right) + \sin\left(\frac{\theta}{2}\right)V \quad (3)$$

Here,  $\theta$  is the rotation angle, and  $V$  is the axis of rotation, a vector on the unit sphere given in cartesian coordinates ( $x,y,z$ ). Notably, unit quaternions span  $SO3$  (i.e. the 4D space of all rotations in 3D), avoiding the degeneracy associated with Euler angle rotations (Shoemaker 1992). Applying sets of random Euler angle rotations does not generate a uniform distribution of orientations in  $SO3$  (i.e., a

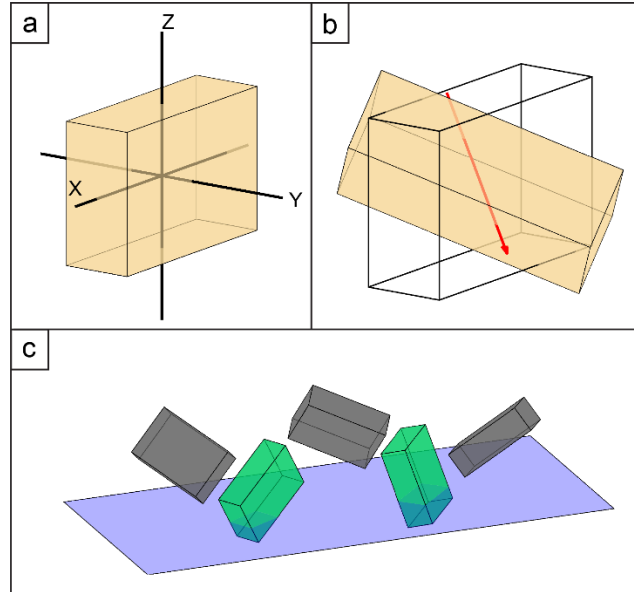


**Fig. 2** Synthetic ODF Algorithm. a) 3D shapes are generated with crystallographic axes tied to coordinate axes. The crystal shape shown is A:3 B:2 C:1. b) After choosing a rotation, the vertices of the 3D shape are rotated, shown here using a unit quaternion (the red vector is the rotation axis defined by the vector portion of the quaternion). c) Rotated shapes are immersed into a volume with cut plane shown in purple. The orientations are collected from the shapes which intersect the cut plane (Green), and discarded when the shapes do not intersect the cut plane (Black)

uniform orientation distribution function, or ODF). The Euler angle approach, while seemingly intuitive, is flawed due to spherical geometry, where random rotations are concentrated towards the poles.

Once a crystal is rotated, the fabric cut effect is accounted for by placing each crystal randomly at a height relative to an intersection plane (Figure 2c). The maximum height relative to the intersection plane is chosen so that each crystal is allowed to miss the intersection plane. If a crystal is cut, that orientation and 2D shape are collected, while if a crystal misses the intersection plane, that crystal and its orientation are discarded.

Orientations of intersected crystals are input into MTEX. Orientation densities are estimated across SO3 using a kernel, or window, function to estimate the ODF. A kernel function is a bounded distribution, equal to zero on either edge at finite points. The kernel function replaces each orientation, and the product of these kernels generates the ODF. The ODF relates the areal proportion (A) of an orientation (r) over the orientation space.

$$ODF(r) = \frac{1}{A} \frac{dA(r)}{dr} \quad (4)$$

A typical choice for the kernel function is the *de la Valée Pouissin* kernel. The selected width of the kernel function has consequences on the resulting ODF estimate. If the kernel width is too small, then the ODF will display large oscillations, with peaks at each discrete orientation, and if the kernel width is too large, the overall fabric is damped. Optimizing the kernel width is performed using the Kullback-Leibler Cross-Validation method (Bachmann et al. 2010; Kullback and Leibler 1951), which tests a range of kernel widths on a randomly selected subset of orientations, selecting the width that best reproduces the omitted orientations in the overall dataset.

Values over the ODF are expressed in terms of multiples of a uniform distribution (MUD). Thus, a genuinely uniform distribution will have a value of  $MUD = 1$  over orientation space. One can conceptualize the ODF as similar to a probability distribution function wrapped over orientation space. In this study, the ODFs are constructed using one orientation measurement per grain rather than orientations per unit area of the 2D crystals (which is analogous to sampling per unit area of the thin section). This choice removes the effect of disperse crystal sizes in the sample, where larger grains would disproportionately impact the resultant fabric analysis due to more sampled orientation points for their larger cross-sectional area.

#### 4) Results

##### 4.1 Fabric -Cut Effect on a Uniform ODF

A crystallographic system needs to be selected to generate synthetic pole figures to visualize the distribution of orientations. To begin, we choose the simple orthorhombic crystal system ( $\alpha = \beta = \gamma = 90^\circ$ ). The resulting pole figures from the Uniform ODF is shown in Figure 3, with  $MUD \approx 1$  across the stereoplot for all axes.

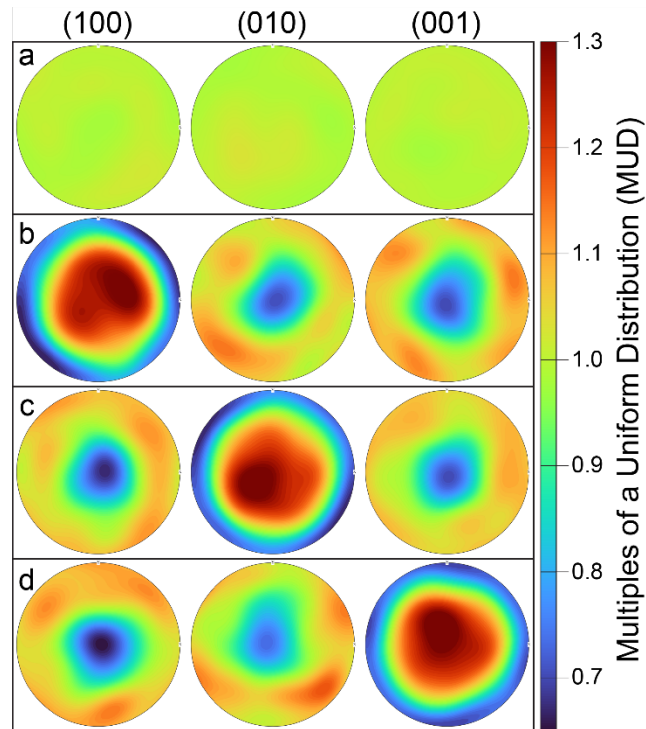


**Fig. 3** ODFs of  $n = 3000$  prolate crystals ( $L = 3, I = S = 1$ ) prior to cutting (a), and after cutting (b-d). Colorbar is in units of Multiples of a Uniform Distribution (MUD) and is equal for all ODFs. a) The true fabric of the system (uncut fabric) displays no discernible structure across each crystallographic axis, with  $MUD \sim 1$ . b) Cut fabric, crystal shape is A: 3, B: 1, C: 1. c) Cut fabric, crystal shape is A: 1, B: 3, C: 1. d) Cut fabric, crystal shape is A: 1, B: 1, C: 3. Note: all cut fabrics display a vertical pole along the corresponding crystallographically controlled long-axis of the crystal, and girdles for the other crystallographic axes

Cutting the crystals that comprise the Uniform ODF results in the development of non-uniform fabric, depending upon the crystal shape (Figure 3). Considering the cut ODF for crystal shape  $A=3$ ,  $B=1$ ,  $C=1$ , the apparent fabric is a vertically aligned pole along the A-axis (and the pole to the face (100)), and horizontal girdles for the B- and C-axes (and the respective poles to faces (010) and (001)). Because the crystal morphology and orientations are controlled as input, the connection between crystal shape and resulting cut fabric can be made, here with the pole perpendicular to the intersection plane coinciding with the crystal long axis ( $A = 3$ ), and girdles for the short axes ( $B = C = 1$ ). From the simple 2D analogy illustrated in Figure 1d, it is clear that the vertical pole for the A-axis, (100), is due to the higher probability of intersecting crystals when the long axis is perpendicular to the intersection plane, skewing the distribution of observed orientations. A simple deduction is that in uniformly distributed orientations, the cut effect results in a pole along the long axis of the crystal. This is further demonstrated in Figure 3 with two other crystal shapes ( $A = 1$ ,  $B = 3$ ,  $C = 1$ , and  $A = 1$ ,  $B = 1$ ,  $C = 3$ ). In each case, the pole is associated with the long axis of the crystal.

While the above treatment demonstrates that the cut effect produces artifacts in the ODF for anisotropic crystal shapes, the results can be made more realistic by taking into consideration the interaxial angles of the commonly analyzed crystal system of plagioclase (triclinic: e.g., Anorthite,  $\alpha = 93.166^\circ$ ,  $\beta = 115.85^\circ$ ,  $\gamma = 91.216^\circ$ ). Plagioclase is the most commonly used phase for textural analyses in igneous rocks due to its near ubiquity in igneous systems and its wide range of crystallization temperatures. These interaxial angles are accounted for in the generation of vertices corresponding to the unrotated crystal. Each crystallographic axis corresponds to a crystallographic face, and so this can be thought of as an untwinned crystal. Accounting for the interaxial angles slightly modifies the resultant pole figures (Figure 4). In this case, the crystal shape is:  $A = 3$ ,  $B = 1$ ,  $C = 1$ . The fabric-cut effect imposes a vertical pole along the A-axis, (100), a horizontal girdle for the B-axis, (010), and a weaker, inclined girdle for the C-axis, (001). The inclination of the C-axis girdle is due to the larger interaxial angle between the A- and C-axes ( $\beta = 115.85^\circ$ ). We note that this fabric-cut effect would also persist for non-uniform ODF scenarios also—except that pole peak and girdle pattern above would be convolved with the underlying non-uniform orientation distribution.

## 4.2 Quantifying the Fabric-Cut Effect

For input uniformly distributed crystal orientations, the fabric-cut effect increases the fabric strength. The magnitude of this effect can be quantified using a texture index. We utilize the J-index to quantify the strength of the fabric (Mainprice et al. 2015). J-Index is defined as:

$$J = \int ODF(r)^2 dr \quad (5)$$

J-Index ranges from 1 (uniformly distributed) to infinity (single crystal fabric). In the following, we propose that the J-Index of a sample can be used to measure whether the underlying fabric is uniform. Several variables need to be constrained: 1) the effect of crystal numbers 2) the effect of crystal symmetry, and 3) the effect of crystal shape.

### 4.2.1 Effect of Crystal Numbers

Sample size (number of crystals) affects the J-Index because we are fitting a continuous ODF to discrete orientation measurements. Fewer measurements can result in poorer fits, resulting in more pronounced fabric. Taken to its extreme, a single crystal orientation will produce a J-Index of infinity, and on the other extreme, approaching an infinite number of crystal orientation measurements will converge on the true texture strength. We test this effect of sample size on texture strength by keeping the crystal shape constant and the orientation distribution uniform, while varying sample size and repeating the process 1000 times for each combination of shape and sample size (Figure 5).

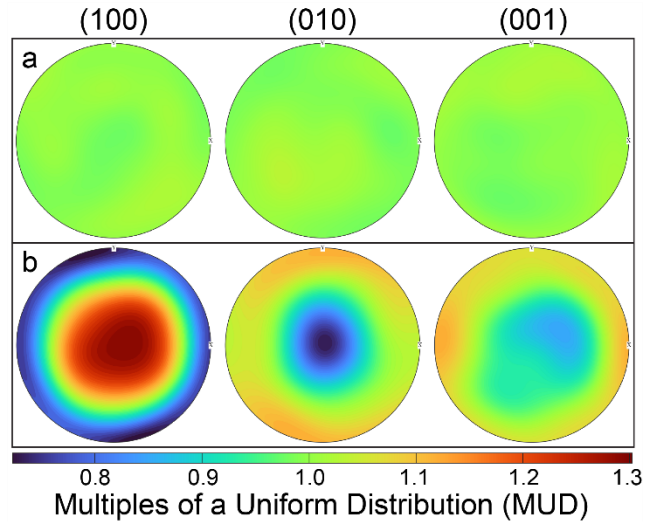


**Fig. 4** ODFs of  $n = 3000$  prolate, triclinic crystals, prior to cutting (a), and after cutting (b). Colorbar is in units of Multiples of a Uniform Distribution (MUD) and is equal for all ODFs. a) The true fabric of the system (uncut fabric) displays no discernible structure across each crystallographic axis, with  $MUD \sim 1$ . b) Cut fabric, crystal shape is A: 3, B: 1, C: 1

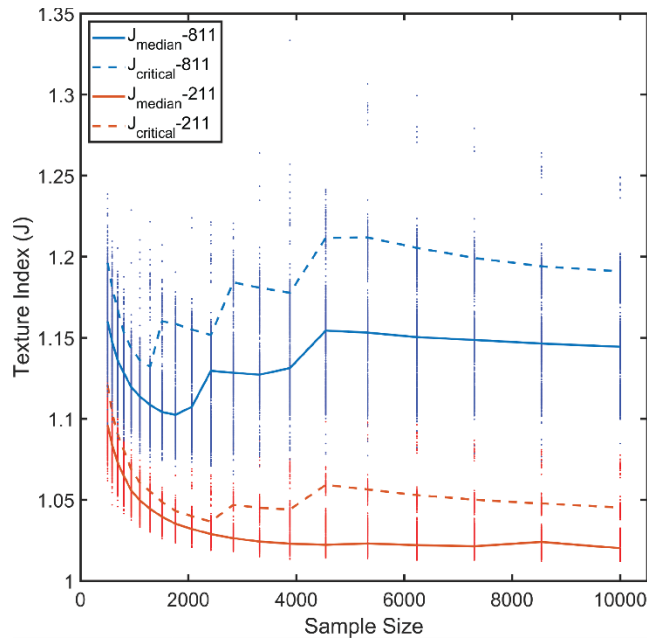


**Fig. 5** Effect of Sample Size on Texture Strength of Cut Fabrics. Blue: ABC = 811, Red: ABC = 211. For each sample size, 1000 runs were performed (datapoints). As observed by the median and critical texture index values, the J-Index generally decreases with increasing crystal count, and asymptotically converges towards the infinite sample size case. Variations in this trend (i.e. the upwards “stair-stepping” in texture index) is an artifact associated with the kernel optimization algorithm, where bandwidth increases and kernel halfwidth decreases with increasing sample size, resulting in slight increases in texture strength

The median texture index for each combination of shape and sample size ( $J_{\text{median}}$ ) and the 95% threshold ( $J_{\text{critical}}$ ) are shown. The impact of the fabric cut effect is most prominent for small sample sizes, while with increasing sample size, asymptotically converges towards a constant as a function of crystal shape. Beyond  $\sim 2000$  crystal orientations sampled, the effect of increasing sample size for a uniform underlying ODF is minimal. Note, that with increasing sample size, there is an additional effect from variations in the optimized kernel halfwidth. As sample size increases, kernel halfwidth tends to decrease, which can result in an increase in measured J-index. These are observed in Figure 5 as “stair-steps” towards increasing sample size. After each of these jumps, however, the overall trend of decreasing J-index with increasing sample size resumes.

#### 4.2.2 Effect of Crystal Symmetry

The effect of the fabric-cut effect on crystal symmetry is tested by comparing orthorhombic crystal symmetry to triclinic crystal symmetry (i.e. plagioclase, as above), by holding both crystal axial ratios and sample size constant ( $n = 3000$  crystals), and repeating the process 1000 times. Results are shown in Figure 6 as a comparison plot by crystal symmetry. Both  $J_{\text{median}}$  and  $J_{\text{critical}}$  fall along a line of slope=1 for very different input crystal shapes, indicating that the crystal symmetry does not play a first-order role in the fabric-cut effect. Although a detailed analysis of the effects of crystal symmetry are beyond the scope of this study, our results suggests that the this is a 2<sup>nd</sup> order effect at best. Thus, our inversion methods (described later) should apply broadly.

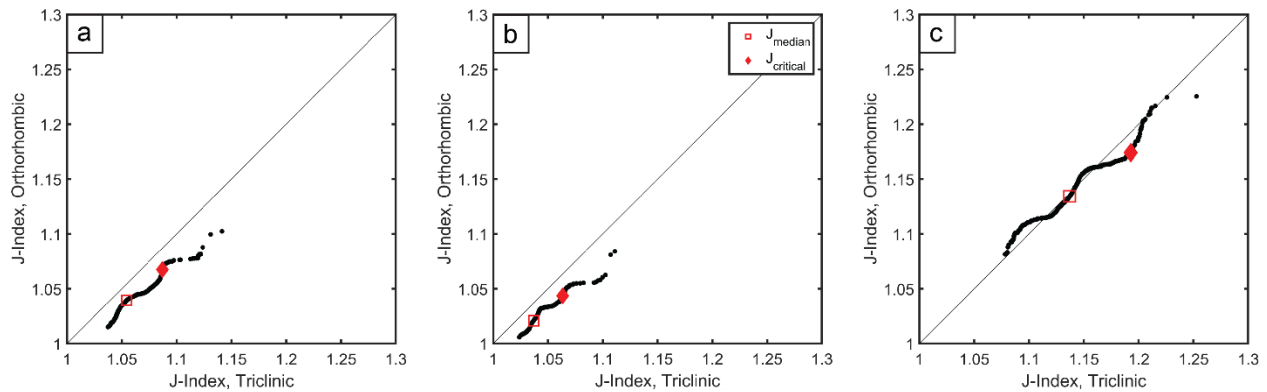


**Fig. 6** Effect of Crystal Symmetry on Texture Strength for 3 crystal morphologies. a) Crystal shape, ABC = 412. b) Crystal shape, ABC = 211. c) Crystal shape, ABC = 811. For each crystal shape, the algorithm is run 1000 times for each crystal morphology and  $n = 3000$  crystals, with results sorted and plotted against each other. There is good agreement in results, with data generally falling near a line of slope 1, indicating that crystal symmetry does not play a strong role in the resulting J-Index, and thus,  $J_{\text{critical}}$

#### 4.2.3 Effect of Crystal Shape

We repeat the same synthetic sectioning analysis as above to test the effect of crystal shape on the resulting cut fabric strength. Crystal shapes are iterated over a wide range of crystal shape space ( $A/C = 0.1:10$ ;  $B/C = 0.1:10$ ), and the sample size is held constant at  $n = 3000$ . The median ( $J_{\text{median}}$ ) and 95% threshold ( $J_{\text{critical}}$ ) values are color coded in Figure 7a and b. In general, as crystal shape becomes more prismatic, the fabric-cut effect becomes more pronounced. The results are roughly the same, independent of which crystal axis is the long axis, and to illustrate this, crystal morphologies are

translated into Zingg-space (Figure 7c) and the morphology of relevant igneous phases plotted (Figure 7d).

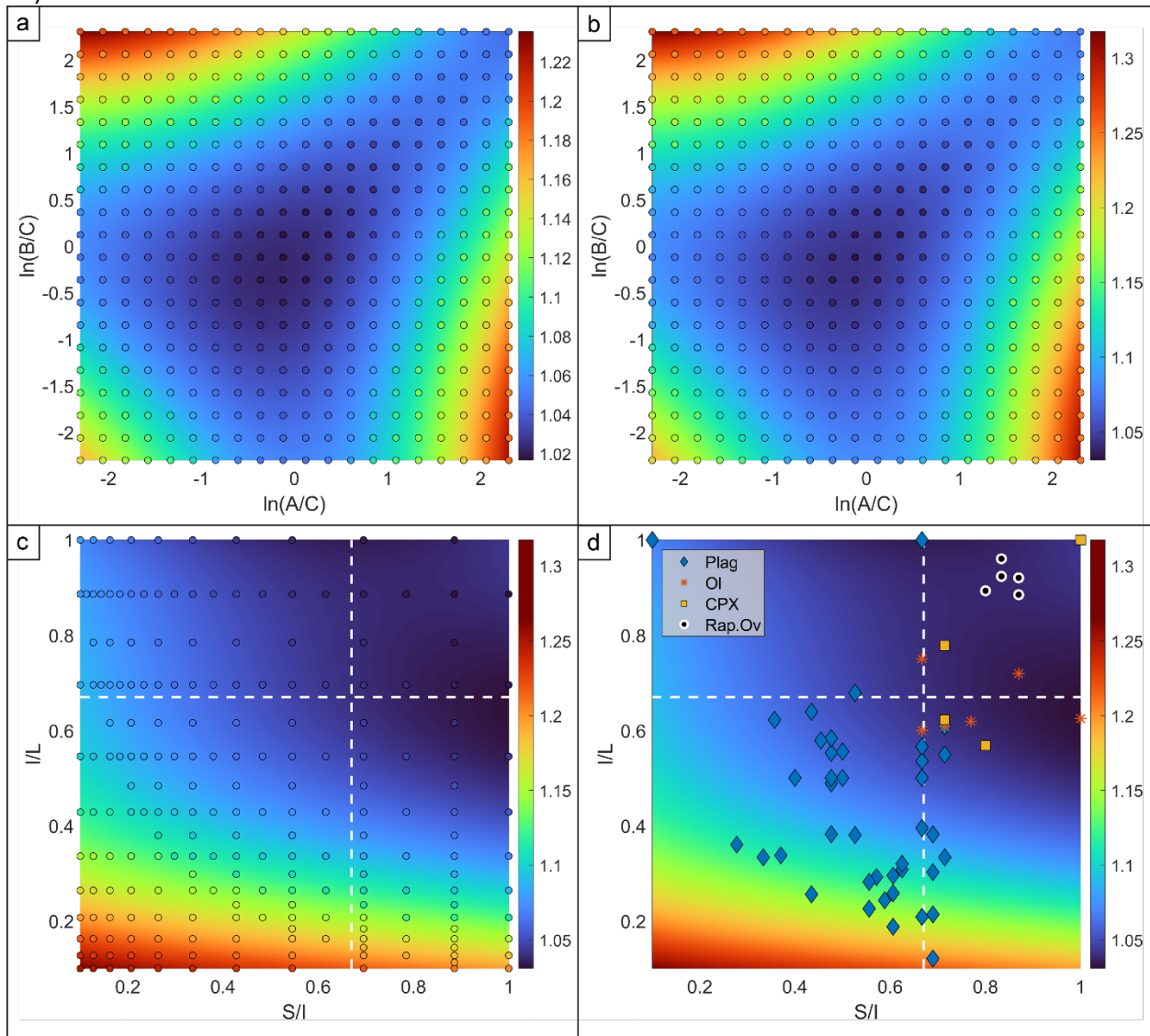


**Fig. 7** Effect of Crystal Shape on Texture Strength. Surfaces fit to results from 1000 runs at each interrogation morphology, with 3000 crystals for each run. Coefficients for the third-order polynomials that describe these surfaces are provided in Table 1. Datapoints in A-C represent are input crystal morphologies, and have been color-coded to the same range as the fit surface (background color). a) Color map of the median texture index value ( $J_{\text{median}}$ ). b) Color map of the 95<sup>th</sup> percentile texture index ( $J_{\text{critical}}$ ). c) Same results as those in B, but translated to Zingg diagram space.  $S/I$  = Short/Intermediate.  $I/L$  = Intermediate/Long. Dashed lines represent divisions in shapes: quadrant I: Equant, II: Plate, III: Blade, IV: Prism. d) Shape estimates for plagioclase, olivine, clinopyroxene, and rapakivied feldspar ovoids (Bain et al., 2019; Brugger and Hammer, 2010; Currier et al., 2019, Higgins, 2002; Magee et al., 2010; Muncill and Lasaga, 1988; Ngonge et al., 2013; Phillips et al., 2013; Salisbury et al., 2008; Vinet and Higgins, 2011)

If crystal shape can be relatively well-constrained, then the J-index of the ODF collected from 2D analysis can be used as an indicator of whether the true, uncut fabric is uniformly distributed. Observing

the range of J-index values, for most crystal shapes, if the J-index of the 2D analysis is greater than  $\sim 1.2$  then the uncut fabric is not uniformly distributed (i.e., there exists a directionally oriented fabric). However, for weaker fabrics, a more precise approach is warranted. To facilitate this process, a 3rd-order polynomial is fit to the results of the fabric-cut effect on crystal shape. The overall fits of these polynomial surfaces are quite good, as indicated by the minimal difference between color-coded datapoints and background polynomial estimation (Figures 7a-c), as well as the large  $R^2$  values ( $J_{\text{median}}$ , Figure 7a:  $R^2 = 0.944$ ;  $J_{\text{critical}}$ , Figure 7b:  $R^2 = 0.946$ ;  $J_{\text{critical}}$ , Figure 7c:  $R^2 = 0.991$ ; ). To utilize this polynomial, coefficients are presented in Table 1, and are input into the following equation:

$$J = C + X + Y + X^2 + XY + Y^2 + X^3 + X^2Y + XY^2 + Y^3 \quad (6)$$

Where values of X and Y depend on whether crystallographic space is considered ( $X = \ln(A/C)$ ,  $Y = \ln(B/C)$ ), or Zingg space is considered ( $X = S/l$ ,  $Y = l/L$ ). The results are interpreted using:

$$\begin{aligned} J \leq J_{\text{critical}}: & \text{ Uniform ODF} \\ J > J_{\text{critical}}: & \text{ ODF is not uniform} \end{aligned}$$

It is important to note that other cut effects (e.g., size distribution), or deviations from our assumptions (e.g. uniform crystal shape) may augment the results presented in this section. For example, if different crystal size populations possess different fabric characteristics, then the size-distribution-cut effect could contribute to the measured ODF.

### 5) Inverting the Fabric Cut Effect

For a single crystal, and considering only the fabric-cut effect, the probability of the crystal intersecting the cut plane is a function of the crystal shape (sh) and crystal orientation (ori). The fabric-cut effect is simply this relationship integrated over all possible orientations. The cut probability,  $p_{\text{cut}}(\text{sh}, \text{ori})$  is taken as the ratio of the vertical profile of an oriented crystal,  $h_{\text{ori}}$ , to the linear distance from the cut plane such that all possible crystal orientations can miss the cut plane,  $h_{\text{max}}$ :

$$p_{\text{cut}} = \frac{h_{\text{ori}}}{h_{\text{max}}} \quad (7)$$

Where  $h_{\text{max}}$  is the maximum distance between antipodal vertices of the crystal, which is the maximum vertical profile for a given crystal shape. The relationship between crystal shape, crystal orientation, and cut probability is illustrated in Figure 8. Note that while the true probability of a crystal intersecting a cut plane will also account for crystal size, this is a consequence of the size-distribution-cut effect. However, assuming that there is no variation in the fabric across crystal sizes, absolute size does not impact this probability.

The intersection probability for each crystal orientation, measured from a cut fabric, is modeled using an input crystal shape. The number of crystals of each orientation in the uncut fabric,  $N_{\text{uncut}}$  (per each observed crystal of a given orientation) is the inverse of the probability of cutting each orientation from the cut fabric.

$$N_{\text{uncut}} = \frac{1}{p_{\text{cut}}} \quad (8)$$

Because crystal numbers are strictly whole numbers, the value of  $N_{\text{uncut}}$  is multiplied by 100 and rounded to generate two significant digits of precision. We choose an uncertainty threshold of  $\sigma = 2.5^\circ$  and apply a three-dimensional Gaussian to blur the inverted orientation slightly. This avoids large crystal

counts of the same orientation. All ODFs generated from these inversions are produced using kernel halfwidths all greater than the chosen  $2.5^\circ$  randomization.

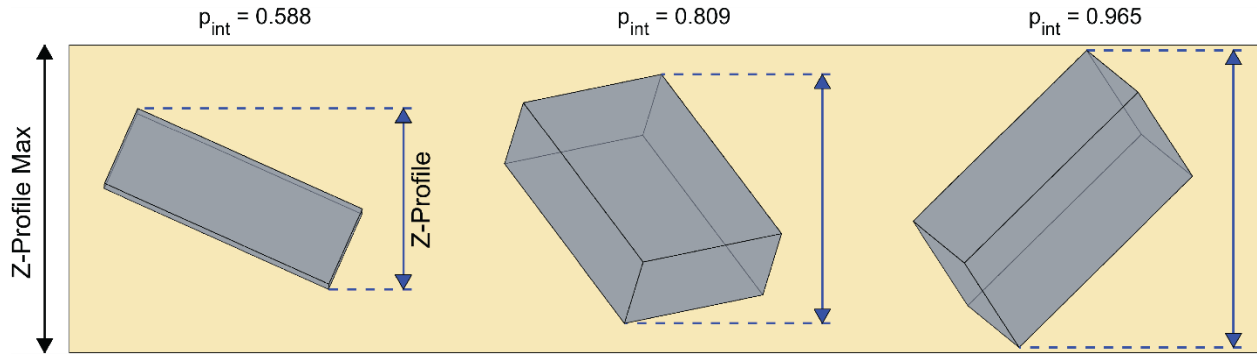


**Fig. 8** Crystal Intersection Probability for three orientations of crystal shape A:3, B:1, C:2. The crystal intersection probability is taken as the ratio of the Z-profile of a crystal to the maximum Z-profile. The maximum Z-profile is a function of the crystal shape, while the Z-profile is a function of both crystal shape and crystal orientation

What we have detailed above assumes a *perfect inversion* scenario. In a natural system, packing effects in a 3D volume will affect these probabilities. So, we also allow for some stochastic variation in the inversion. This *imperfect inversion* method is accomplished by generating a long vector of random numbers sampled from a uniform probability distribution for each associated crystal, and then determining the first element within this array where the random number value is less than each crystal's calculated  $p_{cut}$  value. The count of random numbers necessary to satisfy this condition is taken as  $N_{uncut}$  for the crystal in question. The process follows as in the *perfect inversion* scenario, where orientations are randomized using a three-dimensional Gaussian with  $\sigma = 2.5^\circ$ , and the ODF is constructed. This process is repeated ( $n = 1000$ ), with each repetition an *imperfect inversion* result. Overall, the *imperfect inversion* process is akin to bootstrapping, to estimate the inherent variation associated with the inversion process. Note, that with a large enough number of draws, the average of the stochastic  $N_{uncut}$  values would converge to the  $1/p_{cut}$  case.

The inversion process is tested on two synthetically generated crystal fabrics: 1) a uniform distribution (Figures 9 and 10), and 2) a unimodal (Type-P) distribution (Figures 11 and 12), with the A-axes aligned preferentially near the horizon and to the north. Both modeled systems utilize a constant crystal shape of A:3, B:1, and C:1, with  $n = 3000$  crystals in the cut fabric.

The inverted ODFs presented in Figures 9 and 10 qualitatively illustrate that the inversion methodology is capable of faithfully recreating the uncut fabric. To quantify the inversion fidelity, the J-index and L2 Error between inverted ODFs and the input, uncut fabric are presented in Figures 10 and 12a. As can be observed in the figures, for both the uniform and unimodal fabrics, the cut fabric increases L2 error ( $ODF_{cut} - ODF_{uncut}$ ), and in the case of the uniform fabric, increases the texture index, though it still falls below  $J_{critical}$ . The inversion process decreases the associated L2 error.

The spread in imperfect inversion results indicates the associated error with the inversion process. To test the accuracy of the process, these inverted fabric results can be compared directly against the known uncut fabric used as input. Because the uncut fabric is generated via spherical harmonics, it is essentially equivalent to an infinitely large sample size, which affects texture index (Figure 5). To remove this effect, a similar sample size uncut fabric ( $ODF_{SSS}$ ) is generated by randomly sampling from the infinite sample size uncut fabric ( $ODF_{ISS}$ ). Repeating this process ( $n=1000$ ) allows for

the construction of a 90% confidence interval for both the texture-index (J), and L2 error ( $ODF_{ISS} - ODF_{SSS}$ ). These regions are plotted in blue in Figures 10 and 12a.

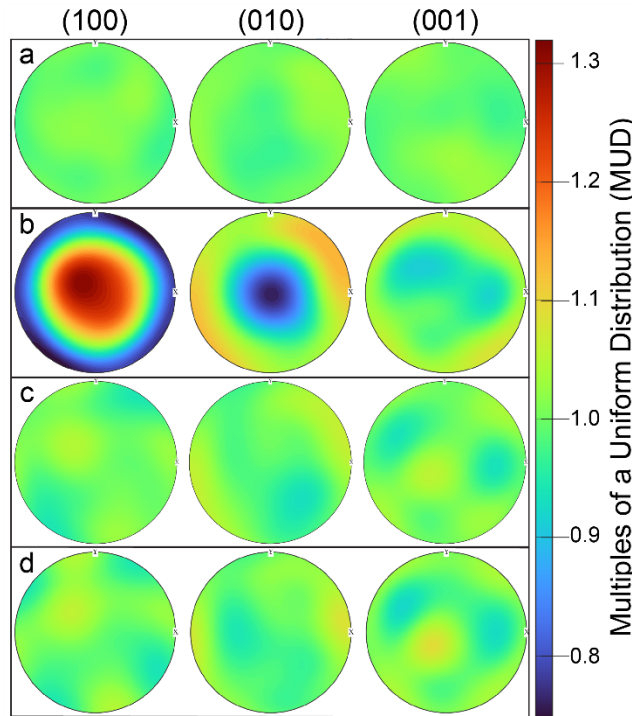


**Fig. 9** Inversion results for synthetically generated and cut uniform fabric, for constant crystal shape  $A = 3$ ,  $B = 1$ ,  $C = 1$ . Colors are coded to MUD, and kept constant for all plots. The inverted ODFs are approximately uniformly distributed ( $MUD \sim 1$  for all orientations). a) Uncut fabric. b) Cut fabric. c) Perfect Inversion. d) Imperfect Inversion

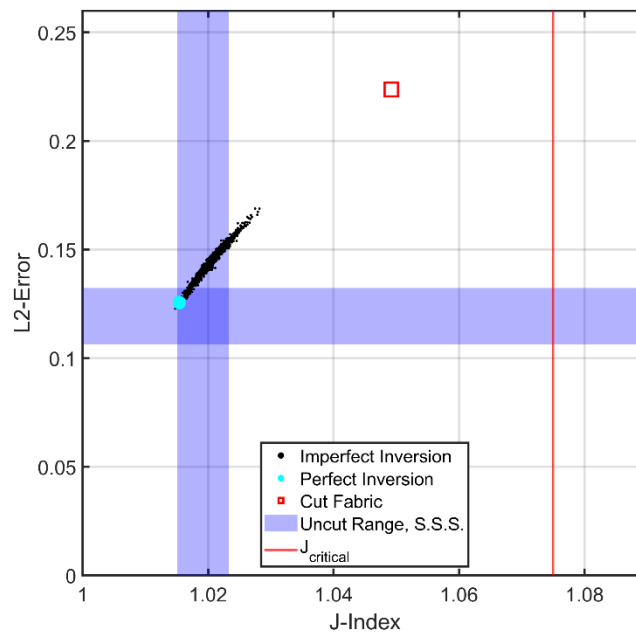


**Fig. 10** Fabric quantification, J-index vs.  $L2_{error} (ODF - ODF_{uncut})$  for the inversions of the synthetic uniform ODF model ( $ABC = 311$ ,  $n = 3000$ ). The uncut fabric ODF is the Uniform ODF, which has a J-index of 1. For a similar sample size ( $n=3000$ ), subsampling from the Uniform ODF generates a 90% confidence interval, with the L2 error measured comparing the similar sample size ODF against the infinite sample size case, uniform ODF (blue region, Uncut Range S.S.S.). The inverted ODFs (black dots ( $n = 1000$ ) and blue circle) reduce L2 Error compared to the cut fabric ODF (red square), and overlap the texture strength of a similar sample size uniform fabric

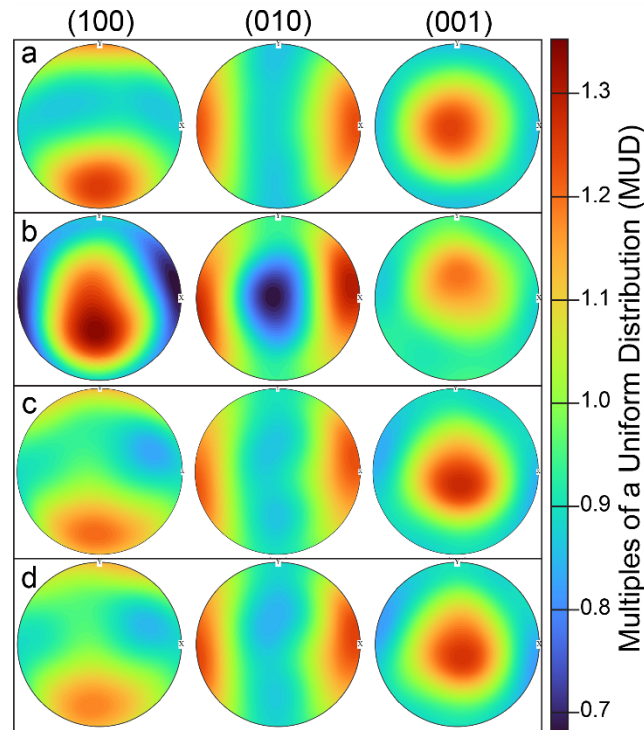


**Fig. 11** Inversion results for synthetically generated and cut unimodal fabric, for constant crystal shape  $A = 3$ ,  $B = 1$ ,  $C = 1$ . Colors are coded to MUD, and kept constant for all plots. a) Uncut fabric with A-axis preferentially aligned to the north of the pole figure. b) Cut fabric, with an apparent fabric that differs from the true, uncut fabric, with A-axes preferentially aligned sub-vertically. c) Perfect Inversion. d) Imperfect Inversion. The inverted ODFs return a good approximation of the uncut fabric

Additionally, for the unimodal, Type-P fabric, the preferred orientation of the inverted fabric can be statistically compared against that of the input fabric (Figure 12B). The fabric-cut effect induces an apparent [100] preferred orientation that is inclined roughly  $55^\circ$  from the horizon. The inversion process recovers the uncut fabric orientation reasonably well, with imperfect inversion confidence intervals, as determined via directional quantile envelope (Kong and Mizera 2012), including the uncut fabric mode.

## 6) Application to Natural Samples

In igneous systems, fabric tends to be relatively weak--significantly weaker than metamorphic systems (Satsukawa et al. 2013). Indeed, much of the EBSD investigations of igneous systems have focused on characterizing and interpreting systems where magmatic fabric is well-developed, such as layered mafic intrusions and cumulate-rich systems (Holness et al. 2012; Cheadle and Gee 2017; Holness et al. 2017; Vukmanovic et al. 2018; Bertolett et al. 2019; Vukmanovic et al. 2019), and fluxion gabbros

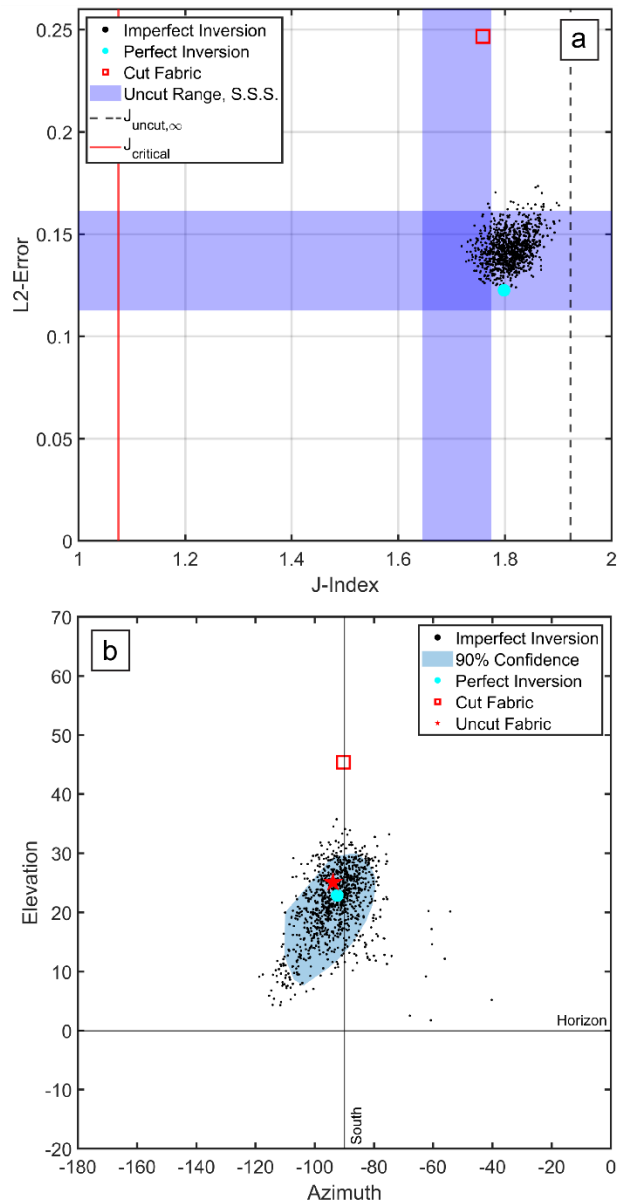


**Fig. 12** Fabric quantification for the inversions of the synthetic Type-P ODF model ( $ABC = 311$ ,  $n = 3000$ ). a) J-index vs.  $L2_{error}$  ( $ODF - ODF_{uncut}$ ). The dashed line is the J-Index for the infinite sample size uncut ODF. For a similar sample size ( $n=3000$ ), subsampling from the Type-P ODF generates a 90% confidence interval, with the L2 error measured comparing the similar sample size ODF against the infinite sample size case, Type-P ODF (blue region, Uncut Range S.S.S.). The inverted ODFs (black dots ( $n = 1000$ ) and blue circle) reduce L2 Error compared to the cut fabric ODF (red square), and imperfect inversions partially overlap the texture strength of the uncut fabric of similar sample size. b) A-Axis mode orientation. The uncut fabric (red star) is approximately oriented to the south (-y direction) with an inclination of 25 degrees. The cut fabric (red square) is inclined at  $\sim 45$  degrees. The inverted ODFs (black dots and blue circle) reduce the associated orientation error. Confidence intervals (blue and pink shaded regions) generated by the imperfect inversions contain the uncut fabric orientation

deep within ophiolite sections (Jousselin et al. 2012; Henry et al. 2021). However, these are exceptional cases, and in igneous systems that have crystallized primarily under static conditions may have little to

no crystal alignment. Alternatively, shearing under granular conditions may result in complex fabrics strongly developed along bands but weakly developed taken in bulk (Fu and Dafalias 2010).

We apply the preceding tools to two separate systems: dolerites from the Basement Sill of Antarctica, and an oriented sample from a feeder dike associated with the Columbia River Flood Basalts and Sill. In these systems, careful interpretation of the observed fabric is essential for determining whether crystallization occurred before flow (i.e., as an entrained load of crystals), or in a static environment, and if a non-uniform fabric exists, accurately determining the directionality of that fabric.

### 6.1 Data Processing

Thin sections were prepared with a probe-quality polish, followed by an EBSD polish that removes any crystallographic strain imparted from the previous cutting and polishing processes. EBSD analyses were collected using a Hitachi S-3400 SEM with an Oxford EBSD system at the Ray and Mary Wilcox SEM Lab of the University of Wisconsin-Madison. The analyses were montaged, large area maps, with an accelerating voltage of 30 keV and specimen tilt of 70 degrees. Step size varied between samples, depending on sample grain size, and are presented in Table 2. EBSD datasets were processed using the MTEX toolkit. While different sets of phases were collected between the natural systems, we focused our attention solely on plagioclase (indexed utilizing the pattern of 'Anorthite' in the Basement Sill, and 'Oligoclase-An28' in the Columbia River Flood Basalt feeder dike). Plagioclase grain boundaries were drawn using the default misorientation threshold of 10°. Polysynthetic twins are identified and merged using misorientations greater than 178°. The average orientation of the merged grain is calculated, and grains smaller than 5 pixels are removed. The orientations of these processed grains are used to generate the cut ODF and resulting J-index. As an aside, the utility of this automated approach is highlighted by the robustness of these datasets, with each sample set in excess of 25000 crystals counted for Antarctic samples, and ~3000 crystals for the Columbia River Flood Basalt Dike (Table 2).

The grain boundaries, represented by a polygon, are measured using principal components. These measurements are input into ShapeCalc to estimate crystal morphology (Mangler et al 2022). This serves as our estimate of crystal shape for comparison of fabric strength against synthetically derived fabric strength. Results are presented in Table 2.

### 6.2 Columbia River Flood Basalt Dike

The Columbia River Flood Basalts are Earth's youngest example of flood basalts (Barry et al. 2013). The main phase of these flows were fed primarily through dikes now residing within the Chief Joseph Dike Swarm, centered on the Wallowa Mountains of Eastern Oregon (Morriss et al. 2020; Petcovic and Grunder 2003; Karlstrom et al. 2019; Reidel and Tolan 2013). Sample PR-1-165 was collected near the margin of a small, ~2m wide dike, located along the "Rattlesnake Gulch" portion of Highway 129 in Southeastern Washington. The sample was collected using a core drill such that the orientation of the resulting thin section is oriented with the long axis along the strike of the dike, and the plane of the thin section aligned along the horizon. Phenocrysts of plagioclase (~1 mm) are present in this dike. Given the width of the dike, it is reasonable to assume that these crystals were present during the emplacement of the dike and thus were capable of recording flow direction via alignment of long-axes sub-parallel to flow direction.

The ODF J-Index exceeds  $J_{critical}$ , indicating that the uncut fabric is non-uniform. Using A: Long and C: Intermediate for an elongate, tabular crystal shape, the inversion process results in a horizontal girdle along the A-axis, (100), and a vertical pole along the B-axis, (010) (Figure 13). The mode for A-axis, (100) orientations of the inverted ODF (Figure 14) reveal a dense grouping along the horizon, but with significant spread at the 90% confidence interval. Considering the inverted ODF (Figure 13), the grouping of [100] orientations along the horizon may seem to suggest lateral flow within the dike, the preferential

grouping along the B-axis, (010), to the vertical, which corresponds to the short axis (B), is inconsistent with this interpretation (i.e. it should be aligned ~perpendicular to the dike margins).

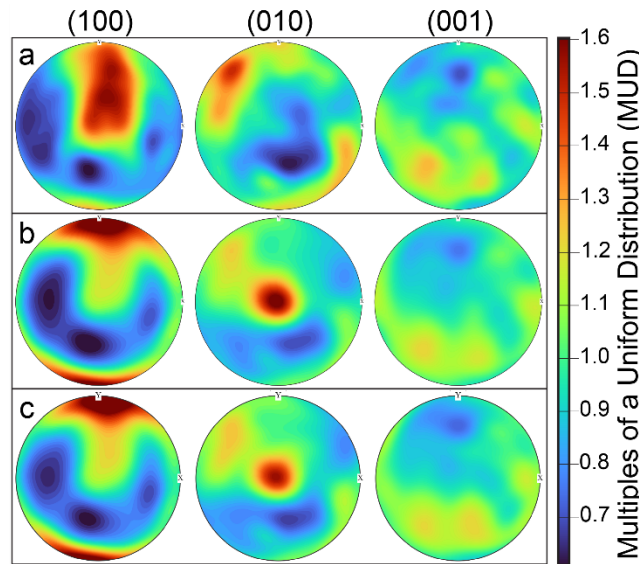


**Fig. 13** Inversion results for PR-1-165. Colors are coded to MUD, and kept constant for all plots. ShapeCalc crystal shape estimate is A: 3.8, B: 1, C: 2.2. a) EBSD derived fabric. Fabric with A-axis preferentially aligned to the north of the pole figure, and sub-vertically arranged. b) Perfect Inversion. c) Imperfect Inversion

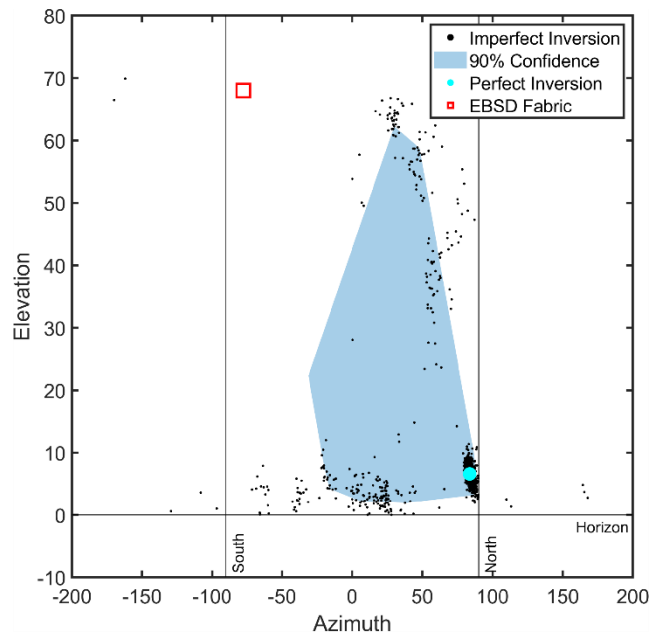


**Fig. 14** ODF mode orientations for the A-Axis of PR-1-165 EBSD data (red square), as well as inversions (black dots and blue circle). The bulk of the imperfect inversion A-Axis mode orientations, as well as the perfect inversion (blue circle) are roughly in the horizontal plane, which is significantly different from the uncorrected apparent EBSD fabric. However, the confidence interval is large, and thus, the true fabric of the rock is poorly constrained

### 6.3 Basement Sill Dolerites

The Basement Sill is a thick mafic intrusion outcropping across much of the McMurdo Dry Valleys of Antarctica. Magmatism here is related to the breakup of Gondwana in the Jurassic, ~180 Ma (Riley and Knight 2001). While the Basement Sill is renowned for its spectacular orthopyroxene and plagioclase crystal tongue the samples utilized here derive from the upper, cumulate-free portion of the sill (Gunn and Warren 1962; Marsh 2004). Due to the large channel width of the Basement Sill (i.e., low shear) and apparent lack of crystal cargo in the upper region, we would not expect to find a discernable rock fabric (e.g. Bird et al. 2002).

EBSD analyses were collected from several dolerite samples near the upper contact of the Basement Sill of Antarctica. These samples were collected in vertical profile, from 0.7 m (ARC-12) 1.7 m (ARC-11), and 2.7 m beneath the contact (ARC-10). The pole figures from these samples appear to reveal a rock fabric (Figure 15). This fabric is relatively uniform across each of the samples, with a vertical pole along the A-axis, a horizontal girdle along the B-axis, and a weaker girdle along C-axis. The alignment is consistent across all three samples.

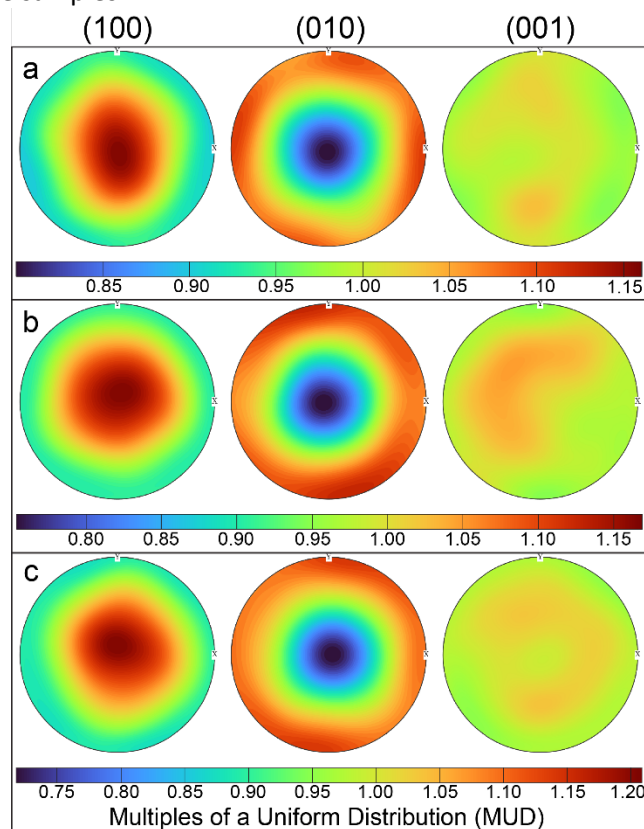


**Fig. 15** Pole Density Figures from Basement Sill Dolerites. Despite samples being collected without orientation preserved, they all display a similar fabric—a vertical pole along (100), a horizontal girdle along (010), and a weaker inclined girdle along (001). a) ARC-10 (2.7 meters beneath contact). b) ARC-11 (1.7 meters beneath contact). c) ARC-12 (0.7 meters beneath contact)

Taken at face value (i.e., without any additional field context), one could interpret this result as either a lineation, if crystals are elongated along the A axis, or a foliation if crystals are tabular, shortened along the A axis (see: Holness et al 2017, their Figure 5), either of which could be significantly important findings for an investigation of physical processes (e.g. flow alignment, or crystal compaction,

respectively). However, these samples were collected unoriented, and thin sectioned at random, so the odds of slicing the rocks in the same manner relative to an underlying fabric are exceedingly slim. Because the measured J-Index is less than  $J_{critical}$ , these observed fabrics can be interpreted as the result of the fabric-cut effect (Table 2). Comparing Figure 15 with Figure 4 allows us to reasonably attach crystal shape to crystallographic axes (A: Long, B: Short, C: Intermediate).

Inverted fabric ODFs are shown for sample ARC-10 in Figure 16. Results were similar for samples ARC-11 and -12. While the  $J\text{-Index} < J_{critical}$  for this sample, the inversion does not result in a uniform ODF, as was the case for synthetically generated crystals (Figure 9). Instead, inverting generates a horizontal girdle along the A-axis, and a vertically inclined pole along the B-axis. These results are eerily similar to that for PR-165 (Figure 13), and suggest that the assumptions built-in to the synthetically generated set of crystals does not hold for this natural system, namely that a single crystal shape can fit the crystal population.

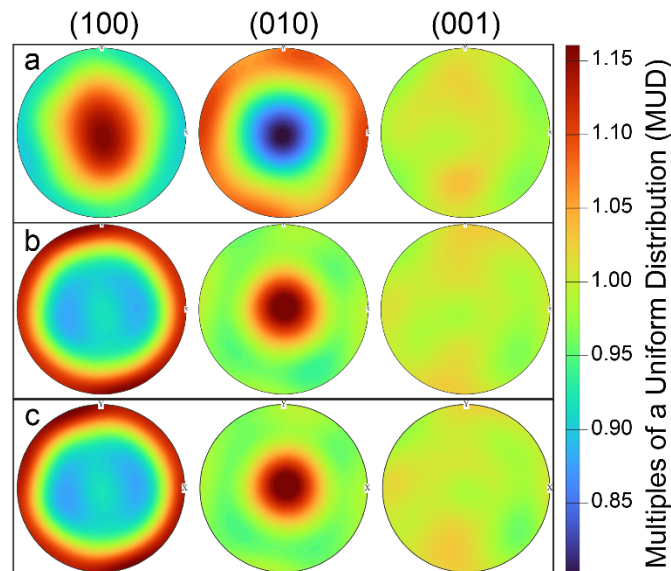


**Fig. 16** Inversion results for ARC-10. Colors are coded to MUD, and kept constant for all plots. ShapeCalc crystal shape estimate is A: 3.6, B: 1, C: 2. a) EBSD derived fabric. Apparent fabric with A-axes preferentially aligned vertically, although  $J < J_{critical}$ . b) Perfect Inversion. c) Imperfect Inversion. Inversions result in a non-uniform fabric, with A-axes forming a girdle, and B-axes forming a vertical pole

From a magmatic perspective, several possible processes that would act to skew the crystal shape population. 1) During crystallization, variations in cooling or decompression rates likely results in variations in crystal shape (Brugger and Hammer 2010; Higgins and Chandrasekharam 2007; Mangler et al. 2022). 2) For persistent phases like plagioclase, which can crystallize over much of the solidification range of magmas as well as over a range of pressures, crystal shapes would become more varied towards the solidus as growth transitions from euhedral in low crystallinity magmas to anhedral in high crystallinity magma. 3) Magma migrating through a complicated magma plumbing system can entrain crystals along their transport path, essentially integrating and homogenizing crystals grown over a range of crystallization regimes (Bergantz et al. 2015; Ganne et al. 2018; Hidalgo et al. 2011; Marsh 2004).

## 7) Discussion

Our results and analysis with synthetic samples directly address the primary motivating question for this study. There are clear stereological biases that can be present when analyzing the crystal orientation datasets from EBSD, i.e. the fabric-cut effect. We also develop and demonstrate a method to invert for this (assuming that it can be decoupled with the shape- and size-cut effect) using just the EBSD data. We

anticipate that this fabric-cut effect is a significant source of bias in systems with weak fabric (e.g., magmatic fabric), or in seemingly strong fabrics at low sample size (Figure 5), but is present in all EBSD orientational data. If meaningful interpretations of dynamic processes are to be made from EBSD derived orientations (Bernard et al. 2023; Casale et al. 2023; Forman et al. 2023; Goudy et al. 2023; Jenkins et al. 2022; Koyama et al. 2023; Levy et al. 2023; Li et al. 2023; Rehman et al. 2023; Vukmanovic et al. 2018; Wiesman et al. 2023), then the fabric-cut effect needs to be corrected for. However, when we apply this method to natural samples, we find that the fabric-cut effect is likely not fully decoupled in a multiplicative manner (i.e., Eq. 1, see more discussion in Section 3). This result suggests some critical challenges with full inversion of underlying 3D rock texture using existing stereological methods.

### **7.1 Towards a comprehensive, open source textural toolkit**

As discussed above and illustrated by some natural samples, the coupled nature of crystal size, crystal shape, and overall fabric indicates that we need new tools with less restrictive assumptions to correctly infer rock texture, with robust uncertainties, from 2D thin sections. In this study, we use synthetic datasets to illustrate a clear conceptual and practical impact of the fabric-cut effect and a robust inversion method, with uncertainties, to correct for it in the synthetic model. However, as an underlying assumption for this analysis is that we can infer a representative crystal size from the data using 2D grain boundary information, using existing tools. When we apply our inversion method, which works correctly for a range of synthetic samples, to natural samples with no reason to possess a preferred orientation (i.e. Basement Sill samples), the results are non-uniform ODFs, suggesting that the constant shape assumption is flawed. This motivates future work toward a textural toolbox that can address the following challenges:

**I) Analysis of model self-consistency:** are we correctly capturing key, first-order processes? In particular, a comprehensive textural toolkit should allow the user to test whether the assumptions inherent in sequential stereological corrections (Eqn 1) apply to their data.

**II) Lack of open-source, well-documented modeling tools:** Although the geoscience community, especially petrology, has been very good at developing open-source codes for stereological analysis of thin sections, some key issues remain. In particular, the modeling codes for generating the synthetic data per each crystal size, and a clear description of assumptions, are unavailable, making it difficult to adapt them for different types of textural analysis. Furthermore, without the source code, it is not easy to assess which particular shape descriptors are best suited for stereological correction (e.g., best-fit ellipse, Feret diameter, bounding rectangle, crystal area, circumference/perimeter, circularity or some subset of them together). It is also challenging to extend the modeling frameworks to include more information such as spatial distribution of the crystals and orientations (in 2D as well as orientation data from EBSD) when performing stereological corrections/inversions. Thus, it is challenging for non-experts to use these methods correctly and modify the codes for different applications. An integrated textural toolbox must be a well-documented, modular, benchmarked, extensible, publicly available model.

An open-source textural analysis toolkit circumvents both of these issues, and there is a need to develop a new toolkit for petrologists interested in textural analyses that fully incorporates data streams from automated methodologies.

## **8) Conclusion**

The EBSD method offers advantages over traditional thin-section-based analyses. Grain measurements are automated and reproducible, and an additional data stream of grain orientation is provided. However, a cut effect skews these results due to the nature of acquiring this orientation data from thin section. We have investigated this effect, and found that it can significantly skew the measured fabric from the true fabric. The fabric-cut effect needs to be accounted for to accurately represent any quantification of fabric collected using EBSD data.

The proper correction for realistic systems is tied to the shape-size-orientation, three-dimensional probability distributions. We have shown the effects in simplified models, but there is no inherent reason for these simplifying assumptions to be true. To more robustly correct for these cut effects, they need to be corrected for simultaneously. The additional orientational data EBSD provides allows for a more accurate inversion compared to 2D thin-section analysis. Still, the bigger picture outcome is that the entire stereological process requires new tools.

TERM	$J_{\text{median}}$ (ABC)	$J_{\text{critical}}$ (ABC)	$J_{\text{critical}}$ (Zingg)
C	1.025	1.045	1.359
X	0.00356	0.004331	-0.9895
Y	0.00578	0.00669	-0.9557
X <sup>2</sup>	0.0132	0.01713	0.05316
XY	-0.01182	-0.01535	-0.1547
Y <sup>2</sup>	0.01378	0.01781	1.222
X <sup>3</sup>	0.002539	0.003433	-0.02731
X <sup>2</sup> Y	-0.005917	-0.007667	0.08967
XY <sup>2</sup>	-0.005889	-0.007608	0.09638
Y <sup>3</sup>	0.00257	0.003501	-0.542
R <sup>2</sup>	0.944	0.946	0.991

**Table 1** Coefficients and associated leading terms of the third-order polynomial surface fit to  $J_{\text{critical}}$  results across crystal morphology space. For crystallographic space:  $X = \ln(A/C)$  and  $Y = \ln(B/C)$ . For Zingg space:  $X = S/l$ ,  $Y = l/L$

SAMPLE	CRYSTAL S	LONG	INTER.	J-INDEX	J <sub>CRIT.</sub>	UNIFORM ?
ARC-10	26354	3.6	2	1.0167	1.0435	Yes
ARC-11	26447	3.6	2.1	1.0186	1.0415	Yes
ARC-12	37900	4.2	2.1	1.0213	1.0424	Yes
PR-1-165	2927	3.8	2.2	1.344	1.0397	No

**Table 2** Results from EBSD analysis of Natural Samples. Crystal shape estimates (Long and Intermediate, with Short = 1) were derived using ShapeCalc (Mangler et al., 2022). When the measured J-Index <  $J_{\text{critical}}$ , the uncut fabric can be assumed to be comprised of uniformly distributed orientations

**Declarations**

**Author Contributions.** All authors contributed to the study conception, study design, and data collection. The first draft was written by Currier, and all authors commented during the evolution of the manuscript. All authors have read and approved the final manuscript.

**Funding.** Support was provided by the National Science Foundation, award number: 2112035

**Financial Interests.** The authors have no financial or proprietary interests in any material discussed in this article.

## References

- Andreani, M., Luquot, L., Gouze, P., Godard, M., Hoise, E., and Gibert, B., 2009. Experimental study of carbon sequestration reactions controlled by the percolation of CO<sub>2</sub>-rich brine through peridotites. *Environmental Science and Technology*, 43, 1226-1231.
- Bachmann, F., Hielscher, R., and Schaeben, H., 2010. Texture analysis with MTEX—Free and open source software toolbox. *Solid State Phenomena* 160, 63-68.
- Bain, A.A., Calder, E.S., Cortes, J.A., Cortes, G.P., and Loughlin, S.C., 2019. Textural and geochemical constraints on andesitic plug emplacement prior to the 2004-2010 vulcanian explosions at Galeras volcano, Colombia. *Bulletin of Volcanology*, 81, 1, 1-25.
- Barry, T.L., Kelley, S.P., Reidel, S.P., Camp, V.E., Self, S., Jarboe, N.A., Duncan, R.A., Renne, P.R., Ross, M.E., Wolff, J.A., and Martin, B.S., 2013. Eruption chronology of the Columbia River Basalt Group. In: *The Columbia River Flood Basalt Province: Geological Society of America Special Paper*, 497, 45-66.
- Bergantz, G.W., Schleicher, J.M., and Burgisser, A., 2015. Open-system dynamics and mixing in magma mushes. *Nature Geoscience*, 8, 10, 793-796.
- Bernard, R.E., Chin, E.J., and Murphy, C., 2023. Melt-assisted deformation in the lower crust of an active plate boundary, Baja California. *Lithos*, 438-439, 106975.
- Bertolett, E.M., Prior, D.J., Gravley, Hampton, S.J., and Kennedy, B.M., 2019. Compacted cumulates revealed by electron backscatter diffraction analysis of plutonic lithics. *Geology*, 47, 445-448.
- Bestmann, M., Prior, D., and Grasemann, B., 2006. Characterisation of deformation and flow mechanics around porphyroclasts in a calcite marble ultramylonite by means of EBSD analysis. *Tectonophysics*, 413, 185-200.
- Bird, R.B., Stewart, W.E., and Lightfoot, E.N., 2002. *Transport Phenomena*, 2<sup>nd</sup> edition. Wiley and Sons, 895 pp.
- Britton, T.B., Jiang, J., Guo, Y., Vilalta-Clemente, A., Wallis, D., Hansen, L.N., Winkelmann, A., and Wilkinson, A.J., 2016. Tutorial: Crystal orientations and EBSD—Or which way is up? *Materials Characterization*, 117, 113-126.
- Brugger, C.R. and Hammer, J.E., 2010. Crystal size distribution analysis of plagioclase in experimentally decompressed hydrous rhyodacite magma. *Earth and Planetary Science Letters*, 300, 246-254.
- Casale, G., Levine, J.S.F., Economou, J., 2023. Extracting quartz deformation fabrics from polymineralic rocks. *Journal of Structural Geology*, 173, 104893.
- Cheadle, M.J., and Gee, J.S., 2017. Quantitative textural insights into the formation of gabbro in mafic intrusions. *Elements*, 13, 409-414.

Cone, K.A., Wendlandt, R.F., Pfaff, K., and Orlandini, O.F., 2020. Texture constraints on crystal size distribution methodology: An application to the Laki fissure eruption. *American Mineralogist*, 105, 5, 585-598.

Cross, A.J., Hirth, G., and Prior, D.J., 2017a. Effects of secondary phases on crystallographic preferred orientation in mylonites. *Geology*, 45, 10, 955-958.

Cross, A.J., Prior, D.J., Stipp, M., and Kidder, S., 2017b. The recrystallized grain size piezometer for quartz: An EBSD-based calibration. *Geophysical Research Letters*, 44, 6667-6674.

Currier, R.M., Ashauer, Z.M., and Norfleet, M.A., 2019. Textural analyses of classical rapakivi granites: Texture formation through coarsening, size-selective replacement, and stirring. *Precambrian Research*, 321, 1-12.

Dunbar, N.W., Jacobs, G.K., and Naney, M.T., 1995. Crystallization processes in an artificial magma: variations in crystal shape, growth rate and composition with melt cooling history. *Contributions to Mineralogy and Petrology*, 120, 412-425.

Etschmann, B., Brugger, J., Pearce, M.A., Ta, C., Brautigan, D., Jung, m., and Pring, A., 2014. Grain boundaries as microreactors during reactive fluid flow; experimental dolomitization of a calcite marble. *Contributions to Mineralogy and Petrology*, 168, 1045, doi:10.1007/s00410-014-1045-z

Farr, R.S., Vukmanovic, Z., Holness, M.B., and Griffiths, E., 2018. Reconstructing grain-shape statistics from electron back-scatter diffraction microscopy. *Physical Review Materials*, 2, 073804.

Forman, L.V., Daly, L., Bland, P.A., Benedix, G.K., and Corrigan, C., 2023. Impacts on the CV parent body: A coordinated, multiscale fabric analysis of the Allende meteorite. *Meteoritics and Planetary Science*, 58, 4, 529-545.

Fossen, H., and Cavalcante, G.C.G., 2017. Shear zones—A review. *Earth-Science Reviews*, 171, 434-455.

Frothingham, M.G., Mahan, K.H., Schulte-Pelkum, V., Goncalves, P., and Zucali, M., 2023. Confronting solid-state shear bias; magmatic fabric contribution to crustal seismic anisotropy. *Geophysical Research Letters*, 50, 6, doi:10.1029/2022GL 102399

Fu, P, and Dafalias, Y.F., 2010. Fabric evolution within shear bands of granular materials and its relation to critical state theory. *International Journal for Numerical and Analytical Methods in Geomechanics*, 35, 1918-1948.

Ganne, J., Bachmann, O., and Feng, X., 2018. Deep into magma plumbing systems: Interrogating the crystal cargo of volcanic deposits. *Geology*, 46, 5, 415-418.

Gibert, B., Seipold, U., Tommasi, A., and Mainprice, D., 2003. Thermal diffusivity of upper mantle rocks: Influence of temperature, pressure, and the deformation fabric. *Journal of Geophysical Research*, 108, B8, 2359, doi:10.1029/2002JB002108

Goudy, S.P., Telus, M., and Chapman, B., 2023. Evidence for multiple early impacts on the H chondrite parent body from electron backscatter diffraction analysis. *Meteoritics and Planetary Science*, 58, 4, 501-515.

Gunn, B., and Warren, G., 1962. Geology of Victoria Land between the Mawson and Mulock Glaciers, Antarctica. *New Zealand Geological Survey Bulletin*, 71, 157 pp.

Haertel, M., and Herwegh, M., 2014. Microfabric memory of vein quartz for strain localization in detachment faults: A case study on the Simplon fault zone. *Journal of Structural Geology*, 68, 16-32.

Hemkemeyer, M., Dohrmann, A.B., Christensen, B.T., and Tebbe, C.C., 2018. Bacterial preferences for specific soil particle size fractions revealed by community analyses. *Frontiers in Microbiology*, 9, doi:10.3389/fmicb.2018.00149

Henry, H., Kaczmarek, M.-A., Ceuleneer, G., Tilhac, R., Griffin, W.L., O'Reilly, S.Y., Gregoire, M., Le Sueur, E., 2021. The microstructure of layered ultramafic cumulates: Case study of the Bear Creek intrusion, Trinity ophiolite, California, USA. *Lithos*, 388-389, 106047.

Hidalgo, P.J., Vogel, T.A., Rooney, T.O., Currier, R.M., and Layer, P.W., 2011. Origin of silicic volcanism in the Panamanian arc: evidence for a two-stage fractionation process at El Valle volcano. *Contributions to Mineralogy and Petrology*, 162, 1115-1138.

Higgins, M.D., 1994. Numerical modeling of crystal shapes in thin sections: Estimation of crystal habit and true size. *American Mineralogist*, 79, 113-119.

Higgins, M.D., 2000. Measurement of Crystal Size Distributions. *American Mineralogist*, 85, 1105-1116.

Higgins, M.D., 2002. A crystal size-distribution study of the Kiglapait layered mafic intrusion, Labrador, Canada: evidence for textural coarsening. *Contributions to Mineralogy and Petrology*, 144, 314-330.

Higgins, M.D. and Chandrasekharam, D., 2007. Nature of sub-volcanic magma chambers, Deccan Province, India: Evidence from quantitative textural analysis of plagioclase megacrysts in the giant plagioclase basalts. *Journal of Petrology*, 48, 5, 885-900.

Holness, M.B., 2014. The effect of crystallization time on plagioclase grain shape in dolerites. *Contributions to Mineralogy and Petrology*, 168, 1076, doi:10.1007/s00410-014-1076-5

Holness, M.B., Sides, R., Prior, D.J., Cheadle, M., Upton, B.G.J., 2012. The peridotite plugs of Rum: Crystal settling and fabric development in magma conduits. *Lithos*, 134-135, 23-40.

- Holness, M.B., Vukmanovic, Z., and Mariani, E., 2017. Assessing the role of compaction in the formation of adcumulates: A microstructural perspective. *Journal of Petrology*, 58, 4, 643-674.
- Holness, M.B., Vukmanovic, Z., and O'Driscoll, B., 2023. The formation of chromite chains and clusters in igneous rocks. *Journal of Petrology*, 64, 1-24.
- Howard, V., and Reed, M.G., 1998. *Unbiased stereology: three-dimensional measurement in microscopy*. Bios Scientific Publishers, Oxford, UK, 246 p.
- Jenkins, M.C., Mungall, J.E., Zientek, M.L., Butak, K., Corson, S., Holick, P., McKinley, R., and Lowers, H., 2022. *Journal of Petrology*, 63, 1-30.
- Jerram, D.A. and Higgins, M.D., 2007. 3D analysis of rock textures: Quantifying igneous microstructures. *Elements*, 3, 239-245.
- Jerram, D.A., Davis, G.R., Mock, A., Charrier, A., and Marsh, B.D., 2010. Quantifying 3D populations, packing and layering in shallow intrusions: A case study from the Basement Sill, Dry Valleys, Antarctica. *Geosphere*, 6, 5, 537-548.
- Jousselin, D., Morales, L.F.G., Nicolle, M., and Stephant, A., 2012. Gabbro layering induced by simple shear in the Oman ophiolite Moho transition zone. *Earth and Planetary Science Letters*, 331-332, 55-66.
- Kang, Q., Lichtner, P.C., Viswanathan, H.S., Abdel-Fattah, A.I., 2010. Pore scale modeling of reactive transport involved in geologic CO<sub>2</sub> sequestration. *Transport in Porous Media*, 82, 197-213.
- Karlstrom, L., Murray, K.E., and Reiners, P.W., 2019. Bayesian Markov-Chain Monte Carlo inversion of low-temperature thermochronology around two 8-10 m wide Columbia River Flood basalt dikes. *Frontiers of Earth Science*, 7, doi:10.3389/feart.2019.00090
- Kong, L. and Mizera, I., 2012. Quantile tomography: Using quantiles with multivariate data. *Statistica Sinica*, 22, 4, 1589-1610.
- Koyama, Y., Wallis, S.R., and Nagaya, T., 2023. Subduction plate interface shear stress associated with rapid subduction at deep slow earthquake depths: example from the Sanbagawa belt, Southwest Japan. *EGUsphere*, 1-33.
- Kullback, S. and Leibler, R.A., 1951. On information and sufficiency. *The Annals of Mathematical Statistics*, 22, 1, 79-86.
- Lanzafame, G., Iezzi, G., Mancini, L., Lezzi, F., Mollo, S., and Ferlito, C., 2017. Solidification and turbulence (non-laminar) during magma ascent: Insights from 2D and 3D analyses of bubbles and minerals in an Etnean Dyke. *Journal of Petrology*, 58, 8, 1511-1533.

- Levy, D.A., Zuza, A.V., Michels, Z.D., and DesOrmeau, J.W., 2023. Buoyant doming generates metamorphic core complexes in the North American Cordillera. *Geology*, 51, 3, 290-294.
- Li, Y., Sun, S., Dong, Y., He, D., Cheng, C., Yang, Z., and Zhang, B., 2023. Rheological behavior of amphibolite facies migmatites during orogenesis: A case study from the North Qinling Belt, China. *Lithos*, 454-455, 107240.
- Magee, C., O'Driscoll, B., and Chambers, A.D., 2010. Crystallization and textural evolution of a closed-system magma chamber: insights from a crystal size distribution study of the Lilloise layered intrusion, East Greenland. *Geological Magazine*, 147, 3, 363-379.
- Mainprice, D., Bachmann, F., Hielscher, R., and Schaeben, H., 2015. Descriptive tools for the analysis of texture projects with large datasets using MTEX: strength, symmetry and components. In: *Rock Deformation from Field, Experiments and Theory*, Faulkner, D.R., Mariani, E., and Mecklenburgh, J. (eds), Geological Society London, 409, 251-271.
- Mangler, M.F., Humphreys, M.C.S., Wadsworth, F.B., Iveson, A.A., and Higgins, M.D., 2022. Variation of plagioclase shape with size in intermediate magmas: a window into incipient plagioclase crystallisation. *Contributions to Mineralogy and Petrology*, 177:64. <https://doi.org/10.1007/s00410-022-01922-9>
- Marsh, B.D., 1998. On the interpretation of crystal size distributions in magmatic systems. *Journal of Petrology*, 39,4,553-599.
- Marsh, B.D., 2004. A magmatic mush column Rosetta Stone: the McMurdo Dry Valleys of Antarctica. *EOS Transactions, American Geophysical Union*, 85, 47, 497-502.
- McLaren, P., 1981. An interpretation of trends in grain size measures. *Journal of Sedimentary Petrology*, 51, 2, 611-624.
- Mock, A., and Jerram, D.A., 2005. Crystal size distributions (CSD) in three dimensions: insights from the 3D reconstruction of a highly porphyritic rhyolite. *Journal of Petrology*, 46, 8, 1525-1541.
- Morgan, D.J., and Jerram, D.A., 2006. On estimating crystal shape for crystal size distribution analysis. *Journal of Volcanology and Geothermal Research*, 154, 1-7.
- Morriss, M.C., Karlstrom, L., Nasholds, M.W.M., and Wolff, J.A., 2020. The Chief Joseph dike swarm of the Columbia River flood basalts, and the legacy data set of William H. Taubeneck. *Geosphere*, 16, 4, 1082-1106.
- Muncill, G.E., and Lasaga, A.C., 1988. Crystal-growth kinetics of plagioclase in igneous systems: isothermal H<sub>2</sub>O-saturated experiments and extension of a growth model to complex silicate melts. *American Mineralogist*, 73 (9-10), 982-992.

Ngonge, E.D., Archanjo, C.J., and Hollanda, M.H.B.M., 2013. Plagioclase crystal size distribution in some tholeiitic mafic dykes in Cabo Frio-Buzios, Rio de Janeiro, Brazil. *Journal of Volcanology and Geothermal Research*, 255, 26-42.

Petcovic, H.L. and Grunder, A.L., 2003. Textural and thermal history of partial melting in tonalitic wallrock at the margin of a basalt dike, Wallowa Mountains, Oregon. *Journal of Petrology*, 44, 12, 2287-2312.

Phillips, J.C., Humphreys, M.C.S., Daniels, K.A., Brown, R.J., and Witham, R., 2013. The formation of columnar joints produced by cooling in basalt at Staffa, Scotland. *Bulletin of Volcanology*, 75:715, doi:10.1007/s00445-013-0715-4.

Polacci, M., Arzilli, F., La Spina, G., Le Gall, N., Cai, B., Hartley, M.E., Di Genova, D., Vo, N.T., Nonni, S., Atwood, C., Llewelling, E.W., Lee, P.D., and Burton, M.R., 2018. Crystallisation in basaltic magmas revealed via in situ 4D synchrotron X-ray microtomography. *Scientific Reports*, 8, 8377, doi:10.1038/s41598-018-26644-6

Poland, M.P., Fink, J.H., and Tauxe, L., 2004. Patterns of magma flow in segmented silicic dikes at Summer Coon volcano, Colorado: AMS and thin section analysis. *Earth and Planetary Science Letters*, 219, 155-169.

Prikryl, R., 2006. Assessment of rock geomechanical quality by quantitative rock fabric coefficients: Limitations and possible source of misinterpretations. *Engineering Geology*, 87, 3-4, 149-162.

Rehman, H.U., Mainprice, D., Barou, F., Yamamoto, H., Wei, C., Zafar, T., and Khan, T., 2023. Crystallographic preferred orientations and microtexture of the Himalayan eclogites revealing records of syn-deformation peak metamorphic stage and subsequent exhumation. *Journal of Structural Geology*, 167, 104792.

Reidel, S.P. and Tolan, T.L., 2013. The Grande Ronde Basalt, Columbia River Basalt Group. In: Reidel, S.P., Camp, V.E., Ross, M.E., Wolff, J.A., Martin, B.S., Tolan, T.L., and Wells, R.E. (eds.), *The Columbia River Flood Basalt Province: Geological Society of America Special Paper*, 497, 117–153.

Riley, T.R. and Knight, K.B., 2001. Age of pre-break-up Gondwana magmatism. *Antarctic Science*, 13, 2, 99-110.

Salisbury, M.J., Bohron, W.A., Clyne, M.A., Ramos, F.C., and Hoskin, P., 2008. Multiple plagioclase crystal populations identified by crystal size distribution and in situ chemical data: Implications for timescales of magma chamber processes associated with the 1915 eruption of Lassen Peak, CA. *Journal of Petrology*, 49, 10, 1755-1780.

Saltikov, S.A., 1967. The determination of the size distribution of particles in an opaque material from the measurement of the size distribution of their sections. In: Elias, H. (Ed.), *Stereology*. Springer-Verlag, NY, pp. 163-173.

Satsukawa, T., Ildefonse, B., Mainprice, D., Morales, L.F.G., Michibayashi, K., and Barou, F., 2013. A database of plagioclase crystal preferred orientations (CPO) and microstructures-implications for CPO origin, strength, symmetry and seismic anisotropy in gabbroic rocks. *Solid Earth*, 4, 511-542.

Shoemaker, K., 1992. Uniform Random Rotations. In: *Graphics Gems III*, Kirk, D. (ed.), Morgan Kaufmann, pp.124-132.

Taylor, J.M., Teyssier, C., Whitney, D.L., McFadden, R.R., and Barou, F., 2023. Linked microstructural and geochemical evolution of mylonitic quartzite during exhumation of a core complex. *Journal of Structural Geology*, 169, 104846.

Underwood, E.E., 1969. Stereology, or the quantitative evaluation of microstructures. *Journal of Microscopy*, 89, 2, 161-180.

Urumovic, K., and Urumovic, K., 2014. The effective porosity and grain size relations in permeability functions. *Hydrology and Earth System Sciences Discussions*, 11, 6675-6714.

Vinet, N., and Higgins, M.D., 2011. What can crystal size distribution and olivine compositions tell us about magma solidification processes inside Kilauea Iki lava lake, Hawaii? *Journal of Volcanology and Geothermal Research*, 208, (3-4), 136-162.

Vukmanovic, Z., Holness, M.B., Monks, K., Anderson, J.C.O, 2018. The Skaergaard trough layering: sedimentation in a convecting magma chamber. *Contributions to Mineralogy and Petrology*, 173. <https://doi.org/10.1007/s00410-018-1466-1>.

Vukmanovic, Z., Holness, M.B., Stock, M.J., and Roberts, R.J., 2019. The creation and evolution of crystal mush in the Upper Zone of the Rustenburg Layered Suite, Bushveld Complex, South Africa. *Journal of Petrology*, 60, 8, 1523-1542.

Wieser, P.E., Vukmanovic, Z., Kilian, R., Ringe, E., Holness, M.B., MacLennan, J., and Edmonds, M., 2019. *Geology*, 47, 948-952.

Wiesman, H.S., Zimmerman, M.E., and Kohlstedt, D.L., 2023. The effect of secondary-phase fraction on the deformation of olivine + ferropericase aggregates: 1. Microstructural Evolution. *Journal of Geophysical Research: Solid Earth*, 128, e2022Jb025723.

Wilkinson, A.J., and Britton, T.B., 2012. Strains, planes and EBSD in materials science. *Materials Today*, 15, 9, 366-376.

Zavada, P., Schulmann, K., Lexa, O., Hrouda, F., Haloda, J., and Tycova, P., 2009. The mechanism of flow and fabric development in mechanically anisotropic trachyte lava. *Journal of Structural Geology*, 31, 1295-1307.